

Investigation of surface topology of printed nanoparticle layers using wide-angle low- Q scattering

Emmanuel O. Jonah,^{a*} Margit Härting,^a Eric Gullikson,^b Andrew Aquila^c and David T. Britton^a

^aNanoSciences Innovation Centre, Department of Physics, University of Cape Town, Rondebosch 7701, South Africa, ^bCenter for X-ray Optics, Lawrence Berkeley National Laboratory, University of California, Berkeley, CA, USA, and ^cEuropean XFEL GmbH, Notkestrasse 85, Hamburg 22607, Germany. *E-mail: emmanuel.jonah@gmail.com

A new small-angle scattering technique in reflection geometry is described which enables a topological study of rough surfaces. This is achieved by using long-wavelength soft X-rays which are scattered at wide angles but in the low- Q range normally associated with small-angle scattering. The use of nanometre-wavelength radiation restricts the penetration to a thin surface layer which follows the topology of the surface, while moving the scattered beam to wider angles preventing shadowing by the surface features. The technique is, however, only applicable to rough surfaces for which there is no specular reflection, so that only the scattered beam was detected by the detector. As an example, a study of the surfaces of rough layers of silicon produced by the deposition of nanoparticles by blade-coating is presented. The surfaces of the blade-coated layers have rough features of the order of several micrometers. Using 2 nm and 13 nm X-rays scattered at angular ranges of $5^\circ \leq \theta \leq 51^\circ$ and $5^\circ \leq \theta \leq 45^\circ$, respectively, a combined range of scattering vector of $0.00842 \text{ \AA}^{-1} \leq Q \leq 0.4883 \text{ \AA}^{-1}$ was obtained. Comparison with previous transmission SAXS and USAXS studies of the same materials indicates that the new method does probe the surface topology rather than the internal microstructure.

Keywords: low- Q scattering; soft X-rays; surface structure; nanostructured materials; printed electronics.

© 2014 International Union of Crystallography

1. Introduction

Small-angle scattering (SAS) is a non-destructive technique which is used for structural analysis of materials. Information such as size, shape, volume and surface areas of the scattering material can be obtained using this technique. SAS is based on the principle that when a collimated beam of a particular wavelength is incident on structures larger than the wavelength of the beam, the intensity of the scattered radiation for low scattering vector Q at angles a few degrees away from the initial trajectory of the beam, below that corresponding to the first diffraction peak, is determined by irregular large-scale variations in the electron density of the material. The classic work on this technique was first developed over 70 years ago (Guinier, 1938), with subsequent works (Porod, 1952; Kratky, 1938; Kratky & Porod, 1949; Debye & Bueche, 1949; Debye *et al.*, 1957) developing the basic methods and the theoretical background that are still used in more advanced experimental methods, including one presented here.

For studies of the inner structures of materials, as well as particles and their agglomerates, using small-angle X-ray scattering (SAXS), the set-up is in transmission mode with the

beam source and detector placed on opposite sides of the sample. In the transmission geometry, the scattered beam originates from the full thickness of the material, which makes SAXS useful for investigating the average internal features of a material, but severely limits its surface sensitivity (Rauscher *et al.*, 1999). SAXS can probe sizes up to about 100 nm using laboratory pinhole collimation instruments (James, 1982; Guinier, 1938; Rauscher *et al.*, 1999). This size range has been extended to hundreds of micrometres in ultra-small-angle X-ray scattering (USAXS) which is based on the Bonse–Hart configuration using a double-crystal monochromator to produce a highly parallel beam (Gullikson *et al.*, 2001). Although USAXS measurements have made use of laboratory X-ray sources (Stark *et al.*, 1998; Rai *et al.*, 2012), they need high-intensity synchrotron sources to achieve practical results (Ilavsky *et al.*, 2009; de Moor *et al.*, 1999).

Variations in structure at nearly atomically flat surfaces can be studied by grazing-incidence SAXS (GISAX) (Levine *et al.*, 1989). However, there is no similar method available for surfaces with large-scale roughness. Unlike conventional SAXS and USAXS, GISAXS is set up in reflection geometry with the beam source and detector located on the same side

of the sample. This technique requires the X-ray beam to be incident on the sample at grazing angles which are comparable with the critical angle for total external reflection of the beam. The interaction between the refracted beam and the features on the sample surface give rise to SAS in the plane of the surface. Another surface-sensitive technique is X-ray reflectometry (XR) (Parratt, 1954; Birkholz, 2006), in which atomic-scale rough features on the surface or at the interface give rise to diffuse scattering, leading to a decrease in intensity in the specularly reflected beam. The most important limitation to both of these techniques is the requirement for a very flat surface (Naudon *et al.*, 1991). For example, using the software available at http://henke.lbl.gov/optical_constants/layer2.html, for a silicon surface with roughness of 1 μm , the reflectivity falls by over nine orders of magnitude within 0.1° from grazing incidence for soft X-rays.

In this paper, we present a low- Q scattering technique using longer-wavelength soft X-rays to study the topology of surfaces with large-scale roughness which cannot be studied by XR or GISAXS. The use of nanometre-wavelength radiation restricts the penetration to a thin surface layer which follows the topology of the surface, while moving the scattered beam to wider angles preventing shadowing by the surface features. The technique is, however, only applicable to rough surfaces for which there is no specular reflection. As an example, a study of the surfaces of rough layers of silicon produced by the deposition of nanoparticles by blade-coating is presented, and the results will be discussed in comparison with measurements of similar materials performed using transmission SAXS and USAXS.

2. Wide-angle low- Q -vector scattering

The principle of the set-up for the experiment is shown in Fig. 1, which has the classical reflection geometry used in X-ray powder diffraction (James, 1982). It uses the same geometry as in a θ - 2θ scan in diffraction experiments to measure scattering of the incident beam from the surface, so as to maintain the direction of the scattering vector \mathbf{Q} perpendicular to the plane of the sample. The basic difference from the above techniques is in the choice of the X-ray wavelength and the minimum angle of incidence. An incident beam with long wavelength is used to probe the sample material at angles greater than its critical angle and generally below the diffraction angle for the first diffraction peak. At the minimum incident angle used with these soft X-rays on surfaces with micrometre-scale roughness, the reflectivity is effectively zero. Hence, this avoids total external reflection from the surfaces, but the low penetration depth for the soft X-rays restricts the observable scattering to the near-surface region. The magnitude of the scattering vector \mathbf{Q} , which is in a direction perpendicular to the substrate, is given as

$$Q = (4\pi/\lambda) \sin(\theta), \quad (1)$$

where λ is the wavelength, the scattering angle is 2θ , and the scattering vector Q is related to the Bragg-like characteristic size d by the relation $d = 2\pi/Q$. In other SAXS experiments,

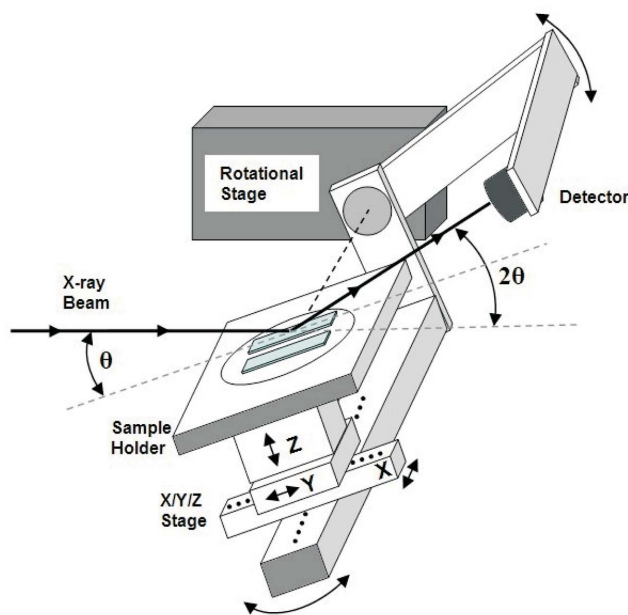
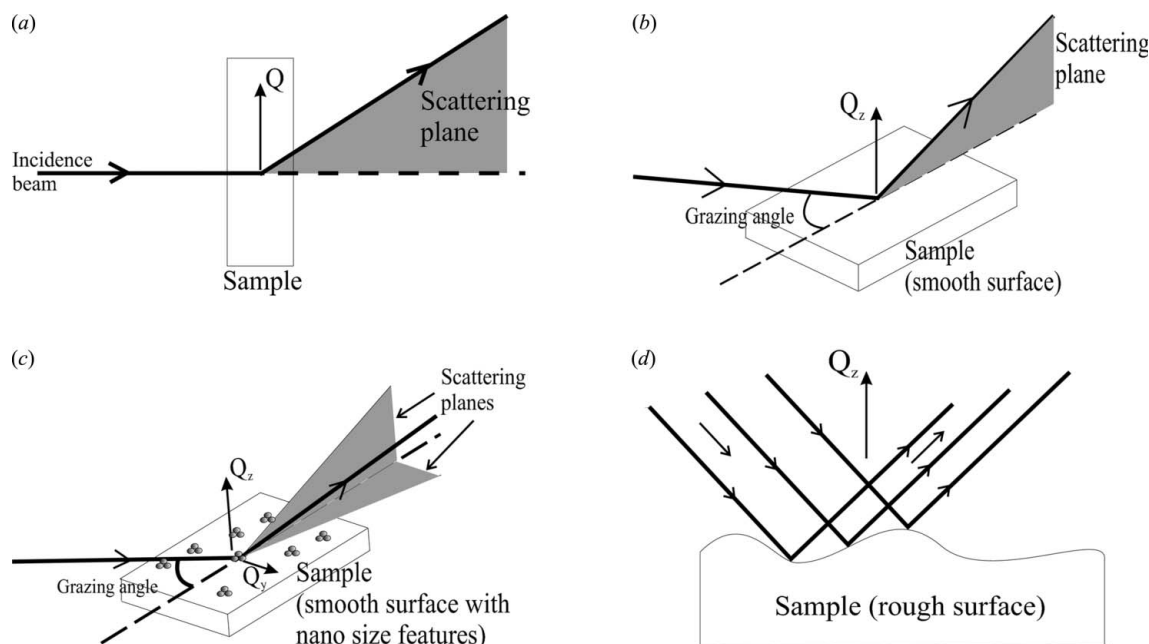


Figure 1
Geometry of the experiment showing the sample stage with strips of samples on wafer and placed on an xyz stage for alignment, with the sample stage and detector moved in a θ - 2θ geometry.

low Q values, corresponding to very large Bragg-like sizes, are obtained with short-wavelength high-energy radiation (8–17 keV) scattered at small angles (Hatton *et al.*, 2005*b*). In contrast, in this experiment, similar Q values are obtained using long-wavelength low-energy radiation scattered at wide angles; hence the description wide-angle low- Q (WALQ). The primary aim is to observe the diffuse scattering features as measured by SAS for bulk material, below the diffraction peaks of a diffraction experiment for the surface of the material under investigation.

The differences between WALQ and other SAS methods are illustrated in Fig. 2. For transmission SAS experiments (Fig. 2*a*), the scattering vector is in a direction perpendicular to the incident beam. There is no momentum transfer, or scattering, in the direction perpendicular to the sample surface (*i.e.* $Q_z = 0$); thus surface features are not investigated (Rauscher *et al.*, 1999). In XR (Fig. 2*b*), the momentum transfer is in a direction perpendicular to the surface of the sample (*i.e.* $Q_z \neq 0$). To obtain significant external reflection, the X-rays have to be incident at grazing angles similar to the critical angle of the material under investigation. This implies not only that only the features that lie on the surface can be investigated, but also that XR can only be performed on samples with near atomically smooth flat surfaces, *i.e.* surfaces with nanometre-scale roughness (Naudon *et al.*, 1991). GISAXS (Levine *et al.*, 1989), shown in Fig. 2(*c*), is slightly different from XR because there is a net momentum transfer both parallel and perpendicular to the surface. Although the GISAXS method can be used to study nanoscale structures on surfaces, it also requires the sample to be similarly smooth to reflectometry, since the beam is also incident at grazing angles less than the critical angle. For the new method of wide-angle


Figure 2

Experimental set-ups for (a) transmission SAS, (b) X-ray reflectometry and (c) GISAXS, showing the scattering planes and how they are different from (d) the WALQ set-up.

low- Q scattering, low-energy X-rays are incident on rough surfaces (Fig. 2d) which have features of the order of several micrometres for which external reflection does not occur. The direction of the momentum transfer of the scattered beam is the same as in XR due to the detector position, but the X-rays are incident at angles greater than the critical angle for total external reflection. Thus, the X-rays penetrate the sample, albeit with a relatively short penetration depth. This is because the low-energy X-rays required for WALQ are easily absorbed by most materials, unlike the high-energy short-wavelength X-rays used in other SAS methods. However, even with this low penetration depth, it has been demonstrated that soft X-rays can be used to study bulk features using resonant diffraction techniques (Hatton *et al.*, 2005a,b). At grazing incidence, shadowing of both the incident and reflected beam may occur depending on the surface feature in Fig. 2(d), especially when the beam is incident on very deep troughs. These effects are prevented in the new method by moving both beams to wider angles, thus enabling scattering of beams off the surfaces of the particles.

3. Experiment

Beamline 6.3.2 of the Advanced Light Source (ALS) Lawrence Berkeley Laboratory (Berkeley, CA, USA) was used in this experiment. The beamline operates in the energy range 50–1300 eV and was originally developed for the characterization of optical elements (Underwood *et al.*, 1996; Underwood & Gullikson, 1998; Gullikson *et al.*, 2001). The beamline has a horizontal- and a vertical-focusing mirror with high focusing ability (Underwood & Gullikson, 1998). A 2 mm × 1 mm beam spot was focused on the samples at normal incidence. The spot size increases laterally in all angles resulting in

an increase in the scattering volume up to a limit determined by the opening angle of the channeltron detector used. Fig. 1 shows the experimental set-up which is a symmetric θ - 2θ configuration. The distance between the sample and the detector is kept fixed, and the sample and detector are rotated in a ratio of 2:1. Thus, in the frame of reference of the sample, the detector and the incident beam are rotated in a circle about a point on the sample surface with a radius equal to the distance between the sample and the detector. The sample stage, along with the detector, is located in a vacuum chamber to avoid scattering and absorption of the soft X-rays in the ambient atmosphere (Bertilson *et al.*, 2007; Kado *et al.*, 1999).

In the selection of the wavelength a balance needs to be achieved between the available scattering angles for the required range of scattering vector and the penetration of the X-rays into the sample material. The penetration depth calculation for silicon at 90°, normal incidence, was obtained using the penetration depth calculator software available at http://henke.lbl.gov/optical_constants/atten2.html, for X-rays of varying wavelength. At a wavelength of 2 nm (~620 eV) the penetration depth of the radiation is about 0.74 μm and the order of magnitude is similar for the 13 nm wavelength (~95 eV) with a penetration depth of 0.54 μm. Thus, the intensity of 2 nm and 13 nm X-rays scattered at angular ranges of $5^\circ \leq \theta \leq 51^\circ$ and $5^\circ \leq \theta \leq 45^\circ$, respectively, was used to investigate the surface structure. Using both wavelengths together yielded a combined range of scattering vector of $0.00842 \text{ \AA}^{-1} \leq Q \leq 0.4883 \text{ \AA}^{-1}$, which covers a Bragg-like size range of $1 \text{ nm} < d < 75 \text{ nm}$. The extension in the size that can be probed is achieved by selecting wavelengths of different energies but similar penetration depth, so as to probe similar areas in the sample. To ensure that there is an overlap in the Q values when selecting multiple wavelengths, the penetration

depth should not be significantly different. For this experiment, the difference of 0.17 μm between the wavelengths was insignificant since the maximum size of 75 nm that could be probed is smaller. Choice of wavelengths that vary significantly in penetration depth could result in loss of information due to discontinuity in the data, or may not even extend the Q range.

Silicon layers similar to those previously investigated using SAXS and USAXS (Britton *et al.*, 2009; Jonah *et al.*, 2012; Rai *et al.*, 2012) were produced by blade-coating on paper substrates. In the earlier studies, the nature of the primary nanoparticles and the topological features of the aggregates formed in the bulk of the layers were investigated. An indication of the surface structure could only be inferred from local information provided by microscopy, as no large-area information could be obtained by scattering. The silicon nanoparticles used in this experiment were obtained from P-type wafers and 2503-grade silicon milled for 5 and 3 h, respectively, using high-energy milling (Britton & Härting, 2006). These are referred to as P-Si and M-Si, respectively, and are similar to those used in the production of printed electronics components such as temperature sensors (Männl *et al.*, 2013), field effect transistors (Härting *et al.*, 2009) and current switching transistors (Britton *et al.*, 2013). A nominally silicon nanopowder (denoted as I-Si) produced by silane pyrolysis obtained from MTI Corporation (Richmond, CA, USA) was also investigated for comparison. For each powder, three inks with different particle concentrations, 80%, 50% and 20% by weight, were produced. The powders were mixed with complementary quantities of a commercial acrylic emulsion, using propan-1,2-diol (propylene glycol) as a thinner to obtain a suitable viscosity. The inks were blade-coated onto 100 μm -thick paper and left to dry under ambient conditions. Fig. 3(a) shows a cross-sectional scanning electron micrograph of a P-Si nanoparticle layer deposited on a paper substrate. A higher magnification view of a section of the surface is shown in Fig. 3(b). The thickness of this section of the printed layer is

about 10 μm with some of the paper fibres protruding through the layer. The surface of the layer is composed of P-Si nanoparticle aggregates of varying sizes forming rough features of the order of several micrometres. Other areas of the layer have different thicknesses, and coverage was not complete with some areas of uncoated paper visible. For the X-ray measurements, the printed samples were cut into strips of 5 cm \times 0.5 cm and mounted onto 4" silicon wafers before mounting in the vacuum chamber of the beamline. A paper sample with no printed silicon layer was also measured as a reference.

3.1. Results and discussion

The relative scattering intensity $I(\theta)$ for each sample was obtained by normalizing the output intensity data with respect to the beam intensity incident on each sample. This was further reduced to $I(Q)$ using the equation

$$I(Q) = I(\theta)(dQ/d\theta)^{-1}, \quad (2)$$

where

$$dQ/d\theta = (4\pi/\lambda)\cos(\theta). \quad (3)$$

This reduction process was used for both the 2 nm and 13 nm wavelengths, and both data combined to give the scattering profile for a sample. A log-log plot of the intensity *versus* Q for the paper substrate and 80% particle loading samples is shown in Fig. 4. The intensities and fits have been scaled by different factors for ease of comparison. The scattering contribution from the substrate, which is also rough, was observed in the scattering data for all the silicon layers as seen in the figure. The oscillation at $Q \simeq 3 \times 10^{-2} \text{ \AA}^{-1}$ in Fig. 4 is a feature which is present in the substrate, and this is also observed in the Si samples because of incomplete coverage of the print layer over the substrate. However, the knee at $Q \simeq 0.1 \text{ \AA}^{-1}$ in all three Si samples was not observed in the substrate scattering data, and is therefore to be interpreted as a feature that arises due to scattering from the nano-

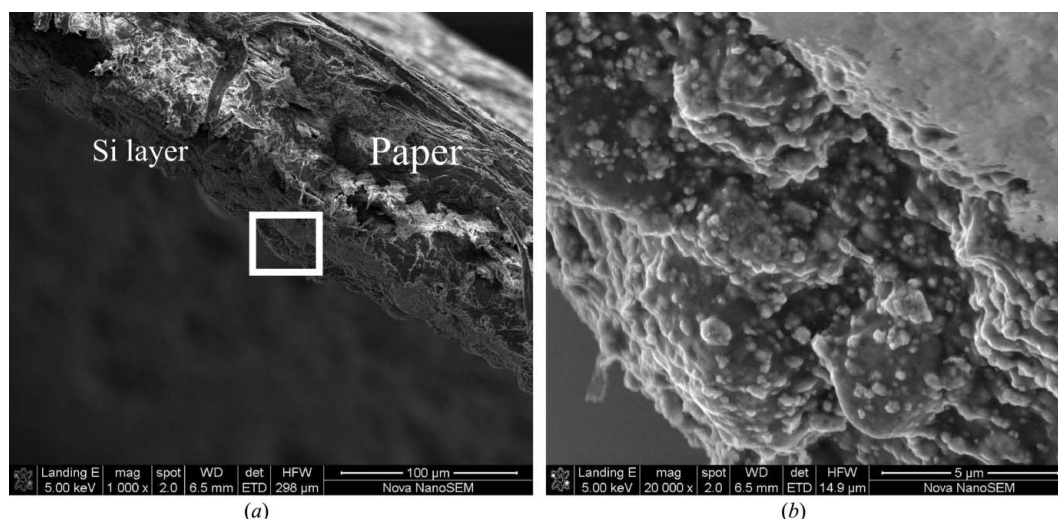


Figure 3

Cross-sectional scanning electron microscope images of (a) P-Si nanoparticle layers deposited on paper, with some paper fibres protruding through the layer, and (b) a higher magnification view of a section of the surface of the layer with rough features of the order of several micrometres.

Table 1

Result from fitting the paper substrate using the unified function [equation (4)] with the third structural level modified with the correlated function [equation (5)] (the power law was not observed for the first level).

Fitting parameters	Level 1	Level 2	Level 3
G	0.52	309.5	4234
B	0	1.0×10^{-6}	5.6×10^{-5}
R_g (Å)	19.1 ± 1.2	67.1 ± 0.7	114.5 ± 7.1
p	–	4	4
ξ (Å)	–	–	177.3 ± 5.4
κ	–	–	8.4

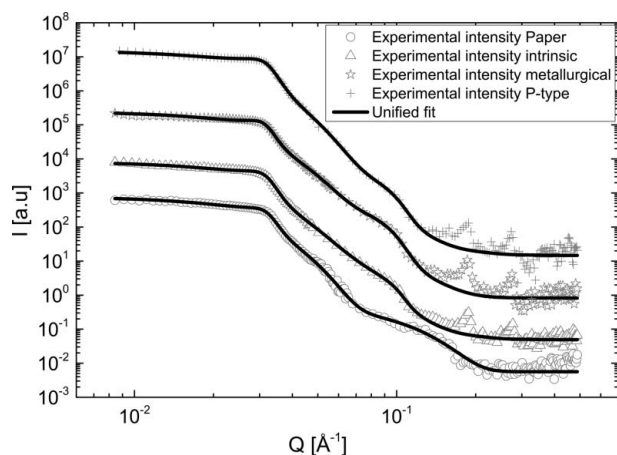


Figure 4

WALQ scattering spectra for the paper substrate (circles), I-Si (triangles), M-Si (stars) and P-Si (crosses). The paper was fitted with three levels of the unified function (solid line) of which the third level was modified with the structure factor equation [equation (5)]. All other samples were fitted with four levels of the unified function, with the second and fourth levels modified with equation (5). The intensities and fits have been scaled by different factors for ease of comparison.

particle layer. Two or more peaks were observed at very high Q ($> 0.158 \text{ \AA}^{-1}$) similar to diffraction peaks of regular structures in the Si samples. These peaks are probably associated with diffraction from the polymer binder and will not be investigated further in this paper which is concerned with the SAS.

Table 2

Results from fitting the unified function [equation (4)] modified with the correlated function [equation (5)] to the scattering data of the silicon nanoparticles.

Sample	Weight (%)	Fitting parameters					
		G	B	p	R_g (Å)	ξ (Å)	κ
I-Si	80	81.04	1.62×10^{-6}	4	49.1 ± 0.3	55.9 ± 0.1	7.94
	50	9.79	3.05×10^{-6}	4	39.9 ± 0.7	67.6 ± 1.3	2.86
	20	8.88	3.83×10^{-6}	4	39.2 ± 0.3	59.7 ± 0.1	4.29
M-Si	80	15.47	3.65×10^{-7}	4	39.5 ± 0.2	57.4 ± 0.1	4.74
	50	157.91	1.09×10^{-6}	4	49.5 ± 0.3	58.1 ± 1.0	8.85
	20	97.22	1.04×10^{-6}	4	51.6 ± 0.4	58.6 ± 0.1	9.02
P-Si	80	16.67	7.44×10^{-7}	4	43.1 ± 0.3	54.6 ± 0.2	5.83
	50	7.00	4.32×10^{-7}	4	39.1 ± 0.7	68.8 ± 1.6	4.19
	20	19.98	4.32×10^{-7}	4	50.0 ± 1.3	60.6 ± 0.1	9.48

The data sets are treated as SAS data relative to the wavelength of the incident radiation since the scattering angles are well below the first diffraction peak for silicon at these wavelengths. The solid line through the data is a fit to the unified function proposed by Beaucage (1995, 1996) describing hierarchical structures of different length scales using

$$I(Q) = \sum_{i=1}^n G_i \exp\left(\frac{-Q^2 R_{gi}^2}{3}\right) + B_i \exp\left(\frac{-Q^2 R_{g(i+1)}^2}{3}\right) \left\{ \frac{[\text{erf}(QR_{gi}/\sqrt{6})]^3}{Q} \right\}^{p_i}, \quad (4)$$

where n is the number of structural levels and $i = 1$ refers to the smallest observable structural level. The first term of equation (4), which is the Guinier function, describes a structure of average size R_{gi} with G_i as the Guinier prefactor. The second term is the Porod function with prefactor B_i and Porod exponent p_i of the same structural level. A modification of the unified function to describe correlated systems (Beaucage *et al.*, 1995) includes a structure function $S(Q)$ which describes the correlation of particles or domains in terms of the interparticle correlation distance ξ and the packing factor κ as

$$S(Q) = \frac{1}{1 + \kappa\theta(Q)} \quad (5)$$

where $\theta(Q)$, which is the structural correlation ‘form factor’, is given as

$$\theta(Q) = 3 \frac{\sin(Q\xi) - Q\xi \cos(Q\xi)}{(Q\xi)^3}. \quad (6)$$

The modified correlated unified function was first used to fit scattered intensity from the paper sample shown in Fig. 4. A broad peak observed in the range $0.00842 \text{ \AA}^{-1} \leq Q \leq 0.03369 \text{ \AA}^{-1}$ is ascribed to particle–particle interference (Rozes *et al.*, 2005). Three structural levels ($n = 3$) of the unified function were used, but only the third level was modified with the function $S(Q)$ in equation (5). The parameters for the fit are given in Table 1. The high- Q power law was not observed, so the Porod prefactor was given a zero value as shown in the table.

The unified equation with $n = 4$ was used to fit all the Si samples with the paper parameters (R_{gi} and p_i) kept fixed for the three levels of the paper, and the fourth level describing the silicon was modified with $S(Q)$ [equation (5)] to fit the broad peak observed in the range $0.0787 \text{ \AA}^{-1} \leq Q \leq 0.1048 \text{ \AA}^{-1}$. A summary of the results obtained for all the samples is shown in Table 2. The radii of gyration obtained ranges from ~ 39 to $\sim 50 \text{ \AA}$ and are independent of the type of silicon nanoparticles in the layer.



Figure 5
Cartoon illustrating an aggregate chain of particles with mass fractal dimension of 1.

These values are too small to correspond to the nanoparticle size since the radii for the I-Si nanoparticles have been shown to be approximately 30 nm (Britton *et al.*, 2009) and for the milled particles to be larger than 40 nm (Jonah *et al.*, 2012). A tentative explanation can be given in terms of the step height between neighbouring particles at the surface. Previous work showed that the aggregates in the bulk of the silicon nanoparticle systems can be described using a branching system, with the minimum path which traverses the aggregate size reported to be a chain with fractal dimension of approximately 1.1 (Jonah *et al.*, 2012; Rai *et al.*, 2012). This dimension is equivalent to a 10% sideways slip of adjacent particles in a chain, which would otherwise have had a dimension of 1 if there were no slip as shown in Figs. 5 and 6. The radii of gyration obtained in this work correspond to about 10% of the size of the nanoparticles, and are related to the height difference between the particles forming the aggregates at the surface. This dip in height is highlighted by the thickness of the horizontal bar shown in Fig. 6(i). If the aggregate length is increased by connecting the three particle units end-to-end, then the height (side slip) and width will change by a factor of approximately 1.1 resulting in a rough structure shown in Figs. 6(ii) and 6(iii) as the stacking procedure is repeated, which has a mass fractal dimension of approximately 1.1. This is an indication that the network of particles on the surface has similar topology as particles in the bulk of the aggregates. The wide area that can be scanned using this technique in a relatively short time is an advantage over complementary techniques such as atomic force microscopy (AFM), that require longer times to scan smaller areas. The very rough surfaces that could be probed with this technique are a disadvantage to AFM because the tips of the probes could be easily damaged. No damage is affected on the surface due to the low beam energy used and no physical contact with surface probes such as the tips of AFM probes. The average distance between the aggregates (ξ) ranges from ~ 55 to ~ 70 Å, thus resulting in a very rough surface composed of similar aggregate features illustrated in Fig. 6(iii).

4. Summary and conclusions

This experiment was performed to show the possibility of using wide-angle low- Q scattering of long-wavelength soft X-rays to study rough surfaces which cannot be studied by any other scattering technique. The use of nanometre-wavelength radiation restricts the penetration to a thin surface layer which follows the topology of the surface, while moving the scattered beam to wider angles preventing shadowing by the surface features. The technique is, however, only applicable to rough surfaces for which there is no specular reflection. By varying

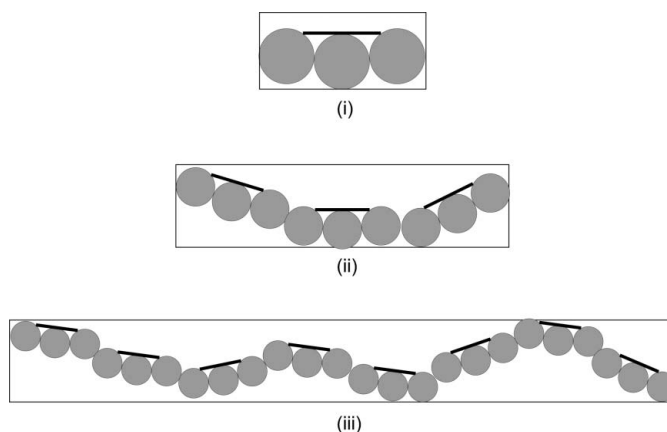


Figure 6
Two-dimensional illustration of the formation of a rough surface from a chain with a mass fractal dimension of 1.1. The thickness of the solid bar shows the 10% dip in the height of adjacent particles as explained in the text with (i) used as the building block for (ii) and (iii).

the energy of the incident X-rays, the penetration depth can be chosen to match the material under investigation and the method does not require any special sample preparation, and hence is non-destructive. Because reflection geometry is used, the thickness of samples is not restricted and both thin films and bulk materials can be studied.

As an example, a study of the surfaces of rough layers of silicon produced by the deposition of nanoparticles by blade-coating was presented. The rough paper substrate was found to have a significant contribution to the scattered intensity for all samples. Comparison with previous transmission SAXS and USAXS studies of the same materials indicates that the new method does probe the surface topography rather than the internal microstructure. Furthermore, the step height obtained from the surface structure is consistent with the topology of the bulk particle aggregates which was only inferred from the previous USAXS studies. These findings are important in fields such as printed electronics where it can be useful in the evaluation of charge transport in composite layers.

This work was supported in part by the NanoPower Africa Project funded by United States Agency for International Development (USAID) through the Higher Education for Development (HED) office. Additional funding to the UCT NanoSciences Innovation Centre was provided by the US Airforce Office of Scientific Research through the project ‘Nanoparticle Solutions for Printed Electronic Applications’, by the University of Cape Town Vice Chancellor’s Strategic Fund, and by the South African National Research Foundation (NRF) under focus area grant FA20064160004. Additional support for the experiments conducted at ALS was provided by the SA Department of Science and Technology (DST) through its Synchrotron Support Programme administered by the NRF. The development of the printed silicon materials was supported by DST through its business unit the Technology Innovation Agency under Technology Advancement Project T50055. We are grateful to Girma G. Goro,

Ntombi Mathe, OluWole D. Solana and Batsirai Magunje for assistance with sample preparation, and to Ayodele Odo and Manfred R. Scriba for assistance with the measurements at ALS.

References

- Beaucage, G. (1995). *J. Appl. Cryst.* **28**, 717–728.
- Beaucage, G. (1996). *J. Appl. Cryst.* **29**, 134–146.
- Beaucage, G., Ulibarri, T., Black, E. & Schaefer, D. (1995). *ACS Symposium Series*, Vol. 585, *Hybrid Organic Inorganic Composites*, ch. 9, pp. 97–111. American Chemical Society.
- Bertilson, M. C., Takman, P. A., Holmberg, A., Vogt, U. & Hertz, H. M. (2007). *Rev. Sci. Instrum.* **78**, 026103.
- Birkholz, M. (2006). *Thin Film Analysis by X-ray Scattering*. New York: Wiley-VCH.
- Britton, D. T. & Härting, M. (2006). *Pure Appl. Chem.* **78**, 1723–1739.
- Britton, D. T., Odo, E. A., Gonfa, G. G., Jonah, E. O. & Härting, M. (2009). *J. Appl. Cryst.* **42**, 448–456.
- Britton, D. T., Walton, S. D., Zambou, S., Magunje, B., Jonah, E. O. & Härting, M. (2013). *AIP Adv.* **3**, 082110.
- Debye, P., Anderson, H. R. & Brumberger, H. (1957). *J. Appl. Phys.* **28**, 679–683.
- Debye, P. & Bueche, A. M. (1949). *J. Appl. Phys.* **20**, 518.
- Guinier, A. (1938). *Nature (London)*, **142**, 569–570.
- Gullikson, E. M., Mrowka, S. & Kaufmann, B. B. (2001). *26th Annual International Symposium on Microlithography*, pp. 363–373. International Society for Optics and Photonics.
- Hatton, P., Wilkins, S., Beale, T., Johal, T., Prabhakaran, D. & Boothroyd, A. (2005a). *J. Magn. Magn. Mater.* **290**, 891–897.
- Hatton, P. D., Wilkins, S. B., Beale, T. A. W., Johal, T. K., Prabhakaran, D. & Boothroyd, A. T. (2005b). *J. Synchrotron Rad.* **12**, 434–441.
- Härting, M., Zhang, J., Gamota, D. R. & Britton, D. T. (2009). *Appl. Phys. Lett.* **94**, 193509.
- Ilavsky, J., Jemian, P. R., Allen, A. J., Zhang, F., Levine, L. E. & Long, G. G. (2009). *J. Appl. Cryst.* **42**, 469–479.
- James, R. W. (1982). *The Optical Principles of the Diffraction of X-rays*. Woodbridge: Ox Bow Press.
- Jonah, E. O., Britton, D. T., Beaucage, P., Rai, D. K., Beaucage, G., Magunje, B., Ilavsky, J., Scriba, M. R. & Härting, M. (2012). *J. Nanopart. Res.* **14**, 1–10.
- Kado, M., Richardson, M., Rajyaguru, J. M., Muszynski, M. J., Friedman, H. & Yamamoto, Y. (1999). *Proc. Soc. Exp. Biol. Med.* **220**, 27–30.
- Kratky, O. (1938). *Naturwissenschaften*, **26**, 94.
- Kratky, O. & Porod, G. (1949). *J. Colloid Sci.* **4**, 35–70.
- Levine, J. R., Cohen, J. B., Chung, Y. W. & Georgopoulos, P. (1989). *J. Appl. Cryst.* **22**, 528–532.
- Männl, U., Chuvilin, A., Magunje, B., Jonah, E. O., Härting, M. & Britton, D. T. (2013). *Jpn. J. Appl. Phys.* **52**, 05DA11.
- Moor, P. E. A. de, Beelen, T. P. M., van Santen, R. A., Tsuji, K. & Davis, M. E. (1999). *Chem. Mater.* **11**, 36–43.
- Naudon, A., Slimani, T. & Goudeau, P. (1991). *J. Appl. Cryst.* **24**, 501–508.
- Parratt, L. (1954). *Phys. Rev.* **95**, 359–369.
- Porod, G. (1952). *Kolloid Z.* **125**, 108–122.
- Rai, D. K., Beaucage, G., Jonah, E. O., Britton, D. T., Sukumaran, S., Chopra, S., Gonfa, G. G. & Härting, M. (2012). *J. Chem. Phys.* **137**, 044311.
- Rauscher, M., Paniago, R., Metzger, H., Kovats, Z., Domke, J., Peisl, J., Pfannes, H.-D., Schulze, J. & Eisele, I. (1999). *J. Appl. Phys.* **86**, 6763.
- Rozes, L., Fornasieri, G., Trabelsi, S., Creton, C., Zafeiropoulos, N., Stamm, M. & Sanchez, C. (2005). *Prog. Solid State Chem.* **33**, 127–135.
- Stark, R. W., Thalhammer, S., Wienberg, J. & Heckl, W. M. (1998). *Appl. Phys. A*, **66**, S579–S584.
- Underwood, J. H. & Gullikson, E. M. (1998). *J. Electron Spectrosc. Relat. Phenom.* **92**, 265–272.
- Underwood, J. H., Gullikson, E. M., Koike, M., Batson, P. J., Denham, P., Franck, K., Tackaberry, R. E. & Steele, W. (1996). *Rev. Sci. Instrum.* **67**, 3372.